HHS Public Access

Author manuscript

Med Phys. Author manuscript; available in PMC 2019 October 01.

Published in final edited form as:

Med Phys. 2018 October ; 45(10): 4652–4659. doi:10.1002/mp.13138.

Technical Note: A benchtop cone-beam x-ray fluorescence computed tomography (XFCT) system with a high-power x-ray source and transmission CT imaging capability

Nivedh Manohar[1,3], **Francisco J. Reynoso**[1,4], and **Sang Hyun Cho**[1,2,*]

[1]Department of Radiation Physics, The University of Texas MD Anderson Cancer Center, Houston, Texas, 77030 USA

[2]Department of Imaging Physics, The University of Texas MD Anderson Cancer Center, Houston, Texas, 77030 USA

[3]Present Address: Department of Radiation Oncology, Winship Cancer Institute of Emory University, Atlanta, GA, 30322 USA

[4]Present Address: Department of Radiation Oncology, Washington University School of Medicine, St. Louis, MO, 63110 USA

Abstract

Purpose: This report describes upgrades and performance characterization of an experimental benchtop cone-beam x-ray fluorescence computed tomography (XFCT) system capable of determining the spatial distribution and concentration of metal probes such as gold nanoparticles (GNPs). Specifically, a high-power (~3 kW) industrial x-ray source and transmission CT capability were deployed in the same platform under the cone-beam geometry.

Methods: All components of the system are described in detail, including the x-ray source, imaging stage, cadmium-telluride detector for XFCT, and flat-panel detector for transmission CT imaging. The general data acquisition scheme for XFCT and transmission CT is also explicated. The detection limit of the system was determined using calibration samples containing water and GNPs at various concentrations. Samples were then embedded in a small-animal-sized phantom and imaged with XFCT and CT. The reconstructed XFCT and CT images were compared and analyzed using the contrast-to-noise ratio for each GNP-containing region of interest. Also, measurements of the incident beam spectra used for XFCT and CT imaging were made and the corresponding x-ray dose rates were estimated, along with the imaging dose.

Results: The present configuration produced a GNP detection limit of 0.03 wt. % with the delivery of an effective dose of 1.87 cGy per projection. XFCT scan of an animal-sized phantom containing low concentrations (down to 0.03 wt. %) of GNP-loaded inserts can be performed within an hour.

*Corresponding author, scho@mdanderson.org.

Disclosure of Conflicts of Interest

The authors have no conflicts to disclose.

Conclusions: The high performance of the system combined with the ability to perform transmission CT in tandem with XFCT suggests that the currently developed benchtop cone-beam XFCT/CT system, in conjunction with GNPs, can be used for routine multimodal preclinical imaging tasks with less stringent dose constraints such as *ex vivo* imaging. With further effort to minimize XFCT imaging dose as discussed in this report, it may also be used for *in vivo* imaging.

Keywords

x-ray fluorescence computed tomography; gold nanoparticles; preclinical imaging; multimodal imaging

1. Introduction

Detection of x-ray fluorescence (XRF) photons followed by tomographic reconstruction is the basis of an imaging modality known as x-ray fluorescence computed tomography (XFCT). XFCT is well-suited for molecular imaging and quantification of high atomic number (Z) materials such as gold nanoparticles (GNPs).[1–3] Especially in the case of GNPs, the relatively high energy of the gold *K*-shell XRF photons (K_α: 68.8 and 67.0 keV) allows XFCT to be a viable option for preclinical imaging of small animals. Typical implementations of XFCT were based on a complex arrangement involving synchrotron x-ray sources and liquid-nitrogen-cooled spectroscopic x-ray detectors.[4–8] Despite distinct advantages (e.g., high system sensitivity for material detection), this type of system has obvious shortcomings (e.g., limited availability, high cost, high dose rate, etc.) for use in routine preclinical small animal imaging. In contrast, benchtop XFCT aimed to use conventional x-ray sources that are widely available, together with room-temperature semiconductor detectors, for a more compact and accessible system. On the other hand, benchtop XFCT also suffers other obstacles due to the polychromatic nature of the x-ray source (e.g., low photon flux for excitation of XRF photons) as well as other technical difficulties (e.g., relatively low energy resolution of room-temperature detectors). Nevertheless, there have been on-going research efforts by many research groups to develop various benchtop XFCT systems[2,3,9–16], since the current research group originally demonstrated the feasibility of benchtop XFCT by imaging of small animal-sized objects containing low (~ 1 wt. %) concentrations of GNPs[1].

This first experimental benchtop XFCT system mentioned above featured a pencil-beam configuration and a low-power (~50 W) x-ray source, resulting in a biologically meaningful but somewhat poor GNP detection limit and an excessively long imaging time.[1] Over the years, similar pencil beam implementations, with both low-power and high-power x-ray sources, have been investigated by other research groups[10–15,17–20], leading to gradual improvement in the performance of pencil-beam benchtop XFCT such as further reduction of photon scatter as well as demonstration of some unique capabilities of benchtop XFCT such as multiplexed imaging of high-*Z* metal probes. Meanwhile, the current research team demonstrated through MC and experimental studies[2,21] that a cone-beam implementation of benchtop XFCT could address the key technical issues noted from the first pencil-beam study, and has continued the development of experimental benchtop XFCT systems adopting the cone-beam geometry.

This technical note details the specifics and challenges of creating a practical stand-alone benchtop cone-beam XFCT system, featuring both a dedicated high-power x-ray source and a flat-panel detector; the latter enables transmission CT imaging capability in the same platform. This report characterizes the performance of the latest system in comparison with previous iterations and also provides insight into some of the obstacles to making benchtop XFCT practical for routine preclinical imaging with GNPs.

2. Materials and Methods

2.A. High-performance benchtop XFCT system

The use of a dedicated x-ray tube, in contrast to the previously-used low-power x-ray source and a high-power *ad hoc* orthovoltage x-ray source used in a recent postmortem animal XFCT imaging study[3], allowed a systematic re-configuration of the entire XFCT system (Figure 1). Comparative specifics and configurations of each of the three sources are shown in Table S-1 of the Supplementary Information.

2.A.1. X-ray source, collimation, and filtration—A high-power x-ray source system (XRS-160, COMET Technologies USA, Inc.) featuring a liquid-cooled, unipolar, tungsten-target (target angle of 20°) x-ray tube (MXR-160/22, COMET Technologies USA, Inc.) was commissioned. The tube had an accelerating potential range of 7.5-160 kVp with a radiation coverage angle of 40°. The focal spot size was user-selectable between 1.0 or 5.5 mm (DIN EN 12543), with respective maximum continuous power ratings of 640 W or 3000 W. The exit window of the tube was 0.8-mm-thick beryllium, which served as inherent filtration. Past the window, a conical collimator (1 cm inlet diameter, 2 cm outlet diameter, 5 cm thickness) was machined out of lead (Pb) and its central axis was aligned with the focal spot of the x-ray beam; the distance from the x-ray source (target) to the collimator inlet was 3.55 cm. If desired, filters of choice could be fitted to the collimator outlet to shape the x-ray spectrum after collimation. Due to the inherent shielding of the x-ray tube, which minimized leakage radiation, no additional shielding was required around it.

2.A.2. Imaging stage—A rotational stage (CR1-Z7, ThorLabs, Inc.), with its center placed 6 cm from the collimator outlet, served as a platform to hold calibration samples or imaging phantoms; the center of the stage was taken to be the isocenter of the XFCT system. The source-to-isocenter distance was therefore 14.55 cm. Radiochromic film (Gafchromic EBT, International Specialty Products, Inc.) was used to verify that the incident x-ray beam had a diameter of at least 3 cm at the isocenter.

2.A.3. Detection components for XFCT—A compact “OEM” version of a thermoelectrically-cooled, energy-resolving, cadmium-telluride (CdTe) detector (AXR-CdTe, Amptek, Inc.) was selected for spectroscopic x-ray detection. The “OEM” version allowed the housing of the detector crystal (5 mm × 5 mm, 1 mm thickness) and preamplifier (PA-230, Amptek, Inc.) to be separated from the power supply (PC5, Amptek, Inc.) and the digital pulse processor / multichannel analyzer (DP5, Amptek, Inc.). The detector featured high detection efficiency in the energy range of interest (~10-100 keV) and also supported processing of high count rates up to 2×10^5 s^{-1}. The manufacturer-specified

energy resolution was < 1.5 keV full-width at half maximum (FWHM) at 122 keV (< 1.23%) and was expected to be approximately 0.7 keV FWHM at 67-69 keV (< 1.03%) under realistic operating conditions.[3] A detector collimator with length of 5 cm and aperture diameter of 2 mm was machined out of SAE grade 304 stainless steel; stainless steel was chosen, rather than lead, to avoid the generation of higher energy lead XRF photons near the detector which may hinder the detection of gold XRF photons. The collimated detector assembly was oriented at 90° with respect to the beam direction and mounted on a translational (horizontal) stage (NRT150, ThorLabs, Inc.); the distance from the isocenter to the plane of the collimator entrance was 5 cm. Additional shielding (1.25-cm-thick lead) was placed around the assembly to limit influx of extraneous photons (i.e., those not arriving via the detector collimator aperture).

2.A.4. Detection components for transmission CT—

A flat-panel x-ray detector (Dexela 1207, PerkinElmer, Inc.), featuring a complementary metal-oxide semiconductor (CMOS) sensor, was commissioned for transmission CT imaging; the detector was optioned with a cesium-iodide (CsI) scintillator due to its high performance (i.e., detection efficiency) in the 12-130 keV energy range. It was placed diametrically opposed to the x-ray source, at a distance of 10 cm from the isocenter of the system. The center of the sensitive area of the detector, a 11.49 cm × 6.46 cm region covered by 1536 × 864 pixels (74.8 μm × 74.8 μm pixel size), was aligned with the central axis of the incident x-ray beam.

2.B. Characterization of system performance

2.B.1. General data acquisition scheme for XFCT and transmission CT—

Both the rotational (imaging) and linear (CdTe detector) stages were controlled by custom software (MATLAB R2015b, The Mathworks, Inc.; Python 3.4.0, Python Software Foundation). The software not only synchronized the movement of the stages but also interfaced with both detectors to seamlessly acquire data (XRF/scatter spectra and transmission images).

The general imaging sequence involved placing the object to be imaged on the rotational stage and centering it at the isocenter of the system. The vertical heights of all the components were adjusted such that the axial slice to be imaged, the incident beam's central axis, the detector collimator aperture, and the center of the flat-panel detector were all located on the same plane (the "imaging plane"). The x-ray source was turned on and scanning began with the CdTe detector field-of-view aligned with the edge of the object closest to the x-ray source. Acquisition of projection data (i.e., 90° XRF/scatter spectra) for XFCT was facilitated by rotation of the imaging stage combined with translation of the CdTe detector stage away from the x-ray source and along the beam direction, to mimic an array detector. Specifically, for each translational position of the CdTe detector, projection data were acquired at desired angular increments over one complete rotation of the object. Meanwhile, the fixed positions of the source and flat-panel detector coupled with the rotation of the object naturally facilitated the acquisition of transmission images at each rotational increment of the object.

2.B.2. Calibration samples and imaging phantom—Commercially-available 1.9-nm-diameter GNPs (AuroVist, Nanoprobes, Inc.) were suspended in phosphate-buffered saline (PBS) to create a stock solution, which was serially diluted to produce additional solutions containing GNPs at 0.01 – 1.0 wt. %. Small containers (6-mm-diameter, 1.5-cm-high) were filled with these solutions; one sample container was filled with PBS only (no GNPs).

As with previous experimental work, a small-animal-sized polymethyl methacrylate (PMMA) phantom was prepared for imaging. The phantom's volume of interest was a 3-cm-diameter, 3-cm-high cylinder into which up to three of the sample containers could be embedded. Two configurations of the phantom were used in this work: one with the phantom loaded with the 0.1, 0.3, and 0.5 wt. % inserts ("high" configuration) and another with it loaded with the 0.03, 0.08, and 0.3 wt. % inserts ("low" configuration).

2.B.3. Detection limit determination—The detection limit of the benchtop XFCT system was determined using the prepared calibration samples (0 – 1.0 wt. %). The x-ray tube was operated at the larger focal spot setting (5.5 mm) which allowed the use of the full 3000 W of power. Based on brief experimental verification of predictions made in a computational study,[22] the accelerating potential was set to 125 kVp and the beam current to 24 mA (maximum possible at 125 kVp); the incident x-ray beam was filtered using a 1.8-mm-thick Sn filter placed after the collimator exit. Each container was placed at the isocenter and irradiated while an XRF/scatter spectrum was acquired with the CdTe detector with an acquisition time of 10 s. After processing the data, the corrected net XRF signals were plotted as a function of GNP concentration. A linear fit was applied to the data to obtain a calibration curve. The detection limit was then defined as the lowest concentration for which the corrected net XRF signals were higher than 1.96 times the standard deviation of the background (95% confidence interval)[23,24].

2.B.4. XFCT and transmission CT imaging of phantom—Although simultaneous XFCT and transmission CT imaging is feasible with the selected imaging geometry, a sequential approach was adopted for this investigation due to the known difficulties[25] of acquiring usable transmission images under irradiation conditions optimized for XFCT. The center of the PMMA phantom's volume of interest was aligned with the imaging plane. XFCT and transmission CT images were acquired for both the "high" and "low" phantom configurations.

For XFCT imaging, the x-ray tube was operated at the same settings as those used for the detection limit determination (125 kVp, 24 mA, 1.8-mm Sn filter, 5.5 mm focal spot setting). The translational step size for the CdTe detector was 3 mm, the rotational step size for the imaging stage was 12°, and the acquisition time per projection was set to 10 s, slightly lower than that used with the *ad hoc* orthovoltage source. A full rotation was performed for a total of 30 projections per translational position. In order to fully cover the width of the phantom, 11 translational positions of the CdTe detector assembly were required for a total of 330 projections.

For transmission CT imaging, the accelerating potential was lowered to 62 kVp and the 1.8-mm-thick Sn filter was replaced with a 0.4-mm-thick Al filter. The x-ray source focal spot size was set to 1.0 mm to maximize image resolution and the beam current was set to 1.0 mA. This configuration was chosen as it resulted in a satisfactory contrast-to-noise ratio based on qualitative analysis of image quality and also for the reason that it would provide a reasonably optimized setting for another mode of benchtop XFCT often known as *L*-shell XFCT or XRF imaging (i.e., XFCT or XRF imaging based on detection of gold *L*-shell XRF photons).[9] Transmission images of the phantom were acquired with the flat-panel CMOS detector for an exposure time of 50 ms per projection at every 1° rotational step over one complete rotation of the phantom; the total number of projections was 360.

2.B.5. Image reconstruction and analysis—XRF/scatter spectra acquired by the CdTe detector were processed by first correcting for detector efficiency and response.[26] Subsequently, the scatter background was fitted with an 8th order polynomial to facilitate extraction of the net (i.e., above background) XRF counts. A Compton-scatter-based attenuation correction algorithm was employed as described in previous work.[3] The corrected XRF signals from each projection were then used with a standard filtered backprojection algorithm to reconstruct an axial XFCT image of the object with 121 pixels (3 mm × 3 mm pixel size) which was smoothed using bicubic interpolation.

The transmission images were flat-field corrected and scaled to obtain projection data. A cone-beam adaptation of the simultaneous iterative reconstruction technique (SIRT) algorithm[27] was used for reconstruction of axial transmission CT images from the projection data. Finally, the axial slice at which the XFCT image was obtained was fused with the transmission CT image of the same slice.

For quantitative analysis (ImageJ, U.S. National Institutes of Health) and comparison between XFCT and transmission CT images, a circular region of interest (ROI) within each imaging insert was established and a contrast-to-noise ratio (CNR) metric was defined as:

$$\mathrm{CNR} = \frac{S_{\mathrm{ROI}} - S_{\mathrm{BKG}}}{\sqrt{\sigma^2_{\mathrm{ROI}} + \sigma^2_{\mathrm{BKG}}}}$$

where S_{ROI} and S_{BKG} are the mean pixel values of an ROI within a GNP-containing insert and an ROI at the center of the phantom (a background region assumed to contain no GNPs), respectively, while σ^2_{ROI} and σ^2_{BKG} are the corresponding variances. For transmission CT images, to account for the inherent radiographic contrast differences between the PMMA of the phantom and PBS, a CNR of 3 was considered to be the detectability threshold.[28]

2.B.6. Incident beam spectra measurements—To characterize the quality of the incident x-ray spectra, the CdTe detector was provisionally relocated to the central axis of the x-ray beam and used to directly measure the x-ray spectra for both XFCT-specific (125 kVp, 1.8-mm Sn filter) and transmission CT-specific (62 kVp, 0.4-mm Al filter) irradiation conditions. For these measurements, the beam current was reduced to the minimum possible

setting (0.5 mA) and the detector was additionally collimated to prevent radiation damage and to reduce the detector dead time.

2.B.7. X-ray dose rate estimation—The x-ray dose rates for both XFCT ($\dot{D}_{XFCT}$) and transmission CT ($\dot{D}_{CT}$) configurations at the isocenter of the system were estimated from ionization chamber measurements using the AAPM TG-61 formalism[29] that was modified as described elsewhere[30] to handle non-standard conditions (in terms of phantom material and x-ray beam size/spectrum). Ionization chamber measurements were performed with a standard Farmer-type ionization chamber (N30013, PTW Freiburg) and an electrometer (DOSE 1, IBA Dosimetry GmbH) using the same PMMA-made dosimetry phantom as used previously[2]. Raw readings from ionization chamber measurements were corrected following the AAPM TG-61 formalism.[29]

2.B.8. Estimation of imaging dose—The dose per transmission CT projection (D^{CT}_{proj}) was simply defined as the product of the time per projection (t^{CT}_{proj}) and the respective dose rate ($\dot{D}_{CT}$):

$$D^{CT}_{proj} = \dot{D}_{CT} \times t^{CT}_{proj}$$

In the case of XFCT imaging, the average observed dead time fraction of the CdTe detector was taken into account to define an effective dose per XFCT projection ($\widetilde{D}^{XFCT}_{proj}$):

$$\widetilde{D}^{XFCT}_{proj} = \dot{D}_{XFCT} \times t^{XFCT}_{proj} \times (1 - \text{Dead Time Fraction})$$

The overall effective imaging dose ($\widetilde{D}_{imaging}$) was then computed using the respective number of projections for each modality (330 for XFCT and 360 for transmission CT):

$$\widetilde{D}_{imaging} = \widetilde{D}^{XFCT}_{proj} \times N^{XFCT}_{proj} + D^{CT}_{proj} \times N^{CT}_{proj}$$

3. Results

3.A. Detection limit

The calibration curve of net XRF signal obtained from each of the calibration samples (0 - 1.0 wt. %) is shown in Figure 2. Note that no net XRF signal was extracted by the signal processing algorithm for XRF/scatter spectra acquired from samples lower than 0.03 wt. %. Therefore, under the current configuration and irradiation parameters, the detection limit was taken to be 0.03 wt. % or 0.3 mg/cm^3. The average dead time fraction during the acquisitions was 55%.

3.B. XFCT and transmission CT imaging performance

For each phantom configuration, the total imaging time was just under 1 hour. Figure 3 shows the reconstructed and smoothed XFCT (left column), transmission CT (right column), and fused (middle column) images of the phantom for both the “high” (top row) and “low” (bottom row) configurations. The reconstructed axial XFCT image demonstrated accurate and specific localization of all the GNP-containing inserts. The signals were mapped to GNP concentration using the calibration curve (Figure 2) and were found to be linear with the expected concentration of each insert. Qualitatively, the locations of the inserts can be visualized in the transmission CT images due mainly to the small air gap surrounding each insert.

Quantitative analysis was performed using the defined CNR metric. The CNR values for each phantom configuration and imaging modality are tabulated in Table 1. S_{BKG} and σ^2_{BKG} for the XFCT images were expectedly 0. All of the inserts were above the detectability threshold (CNR = 3) when imaged with XFCT. However, the three lower concentration inserts (0.03, 0.08, and 0.1 wt. %) had CNR < 3 when imaged using transmission CT. Note, in the present study, the vast majority (98%) of total imaging dose was due to XFCT. Therefore, the CNR comparisons shown here are meant to be merely informative and do not necessarily highlight the superiority of XFCT. (See Section 4 for related discussion).

3.C. Incident beam spectra

Measured incident x-ray spectra for the 125 kVp, 1.8-mm Sn-filtered and 62 kVp, 0.4-mm Al-filtered beams are shown in Figure 4. The figure highlights the difference between irradiation conditions optimized for XFCT and those suitable for transmission CT imaging in terms of the fluence distribution in relation to the *K*-edge of gold (80.7 keV).

3.D. X-ray dose rate and imaging dose

The absorbed dose rates at the isocenter of the system were measured to be 173 and 6694 μGy/mAs for the XFCT (125 kVp, 1.8-mm Sn filter) and transmission CT (62 kVp, 0.4-mm Al filter) incident x-ray spectra, respectively. Imaging dose metrics were subsequently estimated and shown in Table 2. The dose per projection for XFCT and transmission CT were computed to be 1.87 (effective) and 0.0335 cGy, respectively. Taking into account the number of projections for each, the corresponding overall imaging doses, neglecting overhead time, were ~617 (effective) and ~12.1 cGy. This results in an estimated total effective dose (XFCT and transmission CT) of ~629 cGy.

4. Discussion

The main drawback of the original cone-beam XFCT system developed by the current research team was the low photon flux of the x-ray source. The detection limit for GNPs was on the order of 5 mg/cm^3 (0.50 wt. %) for a dose of 0.340 cGy per projection, and the total scan time to image one slice of the 3-cm-diameter PMMA phantom was approximately 6 hours with a single detector used for 11 translational positions. The orthovoltage x-ray source addressed the issue of low photon flux with its 60 times increase in power. The detection limit was lowered by a factor of 2.5 compared to the original configuration,

allowing GNP concentrations as low as 0.24 wt. % to be imaged with a lower dose per projection of 0.207 cGy. Simultaneously, the total scan time was decreased to approximately 1.5 hours (factor of 4 reduction in scan time compared to the original configuration). However, geometrical and physical limitations prevented realization of optimal performance. With the current configuration, the detection limit has been lowered even further, by a factor of 8, to 0.03 wt. % (factor of 16.7 compared to the original configuration) while also realizing an overall scan time reduction from 1.5 hours to 1 hour (factor of 6 compared to the original configuration). Incidentally, the effective dose delivered per XFCT projection using the dedicated system became higher at 1.87 cGy (See Table S-1 and S-2 in Supplementary Information for comparison of the three systems developed by this research team). Nevertheless, the higher dose rate of the current dedicated system allows acquisition time to be reduced considerably. It should be noted that detector limitations prevented full exploitation of the increased dose rate as evidenced by the high dead time fraction (~55%) that was observed. To mitigate dead time, the beam current could be reduced by 45% to allow better use of delivered dose. Therefore, it is clear that in order to fully take advantage of the capabilities of the high-power x-ray source, a more efficient detector capable of handling the higher count rates is needed. This would allow for a substantial reduction in acquisition time while maintaining the same dose per projection.

Under the current setting, the estimated effective XFCT and transmission CT imaging dose of ~629 cGy was much higher than the target dose for *in vivo* small-animal imaging using benchtop XFCT techniques (e.g., 35 cGy). An immediately realizable course of action in limiting the total XFCT dose could involve deploying additional CdTe detectors and reducing the acquisition time per projection. For example, with a total of 6 detectors, the number of projections required would be reduced from 330 to 55. Even assuming the same dead time fraction of 55%, if the irradiation and acquisition parameters were then adjusted such that the effective dose per projection were reduced by 75%, to 0.468 cGy, the total XFCT imaging dose would be 25.7 cGy, and the total imaging time could be on the order of a few minutes. However, the detection limit can be expected to worsen slightly to ~0.06 wt. % under this situation. In order to maintain the detection limit at 0.03 wt. %, it would be necessary to further optimize detector parameters so that the dead time can be minimized while more efficiently acquiring XRF signal.

Concerning transmission CT dose, it needs to be emphasized here that no extensive optimization effort was given to the transmission CT imaging protocol. Thus, with further development and optimization effort, it should be possible to achieve transmission CT dose at least on the order of 1 cGy (or possibly even lower considering the latest advances in micro-CT imaging)[31,32] under a sequential/separate scanning scenario; ideally, a simultaneous XFCT/transmission CT scanning scenario could allow transmission CT imaging to be performed with no additional dose other than what is used for XFCT imaging.

XFCT operates differently from transmission CT in many aspects from signal acquisition to image reconstruction. Thus, the CNR alone might not properly reflect the differences between the two modalities. For example, it is incapable of highlighting the difference between spectroscopic/material-specific (i.e., XFCT) and attenuation-based (i.e., transmission CT) imaging. Nonetheless, the CNR can still be used as a reasonable metric for

comparisons between the two modalities, especially when the CNR per the delivered dose can be calculated more objectively (e.g., through computational studies based on ideal benchtop XFCT setups or after a fully optimized benchtop XFCT system becomes available).

5. Conclusion

In this work, a dedicated kilowatt-power x-ray source was incorporated into an experimental benchtop cone-beam XFCT system. Also, transmission CT capability was added to the current benchtop XFCT system to allow seamless multimodal imaging within the same platform. The detailed system characterization performed in this investigation suggests that the current system, in conjunction with GNPs, can be used for quantitative multimodal (XFCT+CT) preclinical imaging tasks that are not subject to stringent dose constraints (e.g., *ex vivo* imaging). By successfully implementing the XFCT dose reduction strategies as discussed in this report, it may also become ready for *in vivo* imaging.

Supplementary Material

Refer to Web version on PubMed Central for supplementary material.

Acknowledgments

This investigation was supported by the NIH under award numbers R01CA155446 and R01EB020658. The content is solely the responsibility of the authors and does not necessarily represent the official views of the US National Institutes of Health. The authors acknowledge Md Ahmed, Ph.D., Selcuk Yasar, Ph.D., and Luzhen Deng, M.S. for their help with independent verifications of some of the results presented in this study.

References

1. Cheong SK, Jones BL, Siddiqi AK, Liu F, Manohar N, Cho SH. X-ray fluorescence computed tomography (XFCT) imaging of gold nanoparticle-loaded objects using 110 kVp x-rays. Phys Med Biol. 2010;55(3):647–662. [PubMed: 20071757]
2. Jones BL, Manohar N, Reynoso F, Karellas A, Cho SH. Experimental demonstration of benchtop x-ray fluorescence computed tomography (XFCT) of gold nanoparticle-loaded objects using lead- and tin-filtered polychromatic cone-beams. Phys Med Biol. 2012;57(23):N457–467. [PubMed: 23135315]
3. Manohar N, Reynoso FJ, Diagaradjane P, Krishnan S, Cho SH. Quantitative imaging of gold nanoparticle distribution in a tumor-bearing mouse using benchtop x-ray fluorescence computed tomography. Sci Rep. 2016;6:22079. [PubMed: 26912068]
4. Boisseau P Determination of three dimensional trace element distributions by the use of monochromatic x-ray microbeams. Massachusetts Institute of Technology: PhD Dissertation; 1986.
5. Cesareo R, Mascarenhas S. A new tomographic device based on the detection of fluorescent x-rays. Nucl Instrum Meth A. 1989;277(2–3):669–672.
6. Hogan JP, Gonsalves RA, Krieger AS. Fluorescent computer tomography: a model for correction of x-ray absorption. IEEE Trans Nucl Sci. 1991;38(6):1721–1727.
7. Takeda T, Ito K, Kishi K, et al. Preliminary experiment of the fluorescent X-ray computed tomography with synchrotron radiation. Jpn J Med Imaging Tech. 1994;12:537–538.
8. Takeda T, Akiba M, Yuasa T, et al. Fluorescent x-ray computed tomography with synchrotron radiation using fan collimator. Proc SPIE 2708, Medical Imaging 1996: Physics of Medical Imaging 1996:685–695.
9. Manohar N, Reynoso F, Cho SH. Feasibility of direct L-shell fluorescence imaging of gold nanoparticles using a benchtop x-ray source. Med Phys. 2012;39(6):3987–3988.

10. Kuang Y, Pratx G, Bazalova M, Qian J, Meng B, Xing L. Development of XFCT imaging strategy for monitoring the spatial distribution of platinum-based chemodrugs: instrumentation and phantom validation. Med Phys. 2013;40(3):030701. [PubMed: 23464279]
11. Kuang Y, Pratx G, Bazalova M, Meng B, Qian J, Xing L. First demonstration of multiplexed x-ray fluorescence computed tomography (XFCT) imaging. IEEE Trans Med Imag. 2013;32(2):262–267.
12. Ren L, Wu D, Li Y, Wang G, Wu X, Liu H. Three-dimensional x-ray fluorescence mapping of a gold nanoparticle-loaded phantom. Med Phys. 2014;41(3):031902–n/a. [PubMed: 24593720]
13. Bazalova-Carter M, Ahmad M, Xing L, Fahrig R. Experimental validation of L-shell x-ray fluorescence computed tomography imaging: phantom study. J Med Imaging. 2015;2(4):043501.
14. Groll A, George J, Vargas P, La Rivière PJ, Meng LJ. Element mapping in organic samples utilizing a benchtop x-ray fluorescence emission tomography (XFET) system. IEEE Trans Nucl Sci. 2015;62(5):2310–2317. [PubMed: 26705368]
15. Ricketts K, Guazzoni C, Castoldi A, Royle G. A bench-top K X-ray fluorescence system for quantitative measurement of gold nanoparticles for biological sample diagnostics. Nucl Instrum Meth A. 2016;816(Supplement C):25–32.
16. Dunning CAS, Bazalova-Carter M. Sheet beam x-ray fluorescence computed tomography (XFCT) imaging of gold nanoparticles. Med Phys. 2018;45(6):2572–2582. [PubMed: 29604070]
17. Bazalova M, Kuang Y, Pratx G, Xing L. Investigation of x-ray fluorescence computed tomography (XFCT) and K-edge imaging. IEEE Trans Med Imag. 2012;31(8):1620–1627.
18. Sjölin M, Danielsson M. Improved signal-to-noise ratio for non-perpendicular detection angles in x-ray fluorescence computed tomography (XFCT). Phys Med Biol. 2014;59(21):6507. [PubMed: 25310695]
19. Ahmad M, Bazalova M, Xiang L, Xing L. Order of magnitude sensitivity increase in X-ray Fluorescence Computed Tomography (XFCT) imaging with an optimized spectro-spatial detector configuration: theory and simulation. IEEE Trans Med Imag. 2014;33(5):1119–1128.
20. Vernekohl D, Tzoumas S, Zhao W, Xing L. Polarized x-ray excitation for scatter reduction in x-ray fluorescence computed tomography. Med Phys. 2018.
21. Jones BL, Cho SH. The feasibility of polychromatic cone-beam x-ray fluorescence computed tomography (XFCT) imaging of gold nanoparticle-loaded objects: a Monte Carlo study. Phys Med Biol. 2011;56(12):3719. [PubMed: 21628767]
22. Manohar N, Jones BL, Cho SH. Improving x-ray fluorescence signal for benchtop polychromatic cone-beam x-ray fluorescence computed tomography by incident x-ray spectrum optimization: A Monte Carlo study. Med Phys. 2014;41(10):101906. [PubMed: 25281958]
23. Ricketts K, Castoldi A, Guazzoni C, et al. A quantitative x-ray detection system for gold nanoparticle tumour biomarkers. Phys Med Biol. 2012;57(17):5543–5555. [PubMed: 22871575]
24. Manohar N, Reynoso FJ, Cho SH. Experimental demonstration of direct L-shell x-ray fluorescence imaging of gold nanoparticles using a benchtop x-ray source. Med Phys. 2013;40(8):080702. [PubMed: 23927295]
25. Manohar N, Cho SH. Quality of micro-CT images acquired from simultaneous micro-CT and benchtop x-ray fluorescence computed tomography (XFCT): A preliminary Monte Carlo study. Nuclear Science Symposium and Medical Imaging Conference (NSS/MIC), 2013 IEEE 2013:1–3.
26. Reynoso FJ, Tailor R, Wang CC, Cho SH. Comparison of filtered x-ray spectra and depth doses derived from a hybrid Monte Carlo model of an orthovoltage x-ray unit with experimental measurements. Biomed Phys Eng Express. 2016;2(4):045011.
27. Gilbert P Iterative methods for the three-dimensional reconstruction of an object from projections. J Theor Biol. 1972;36(1):105–117. [PubMed: 5070894]
28. Rose A Vision: Human and Electronic. New York - London: Plenum Press; 1973.
29. Ma CM, Coffey CW, DeWerd LA, et al. AAPM protocol for 40–300 kV x-ray beam dosimetry in radiotherapy and radiobiology. Med Phys. 2001;28(6):868–893. [PubMed: 11439485]
30. Jones BL. Development of dosimetry and imaging techniques for pre-clinical studies of gold nanoparticle-aided radiation therapy. Georgia Institute of Technology: PhD Dissertation; 2011.
31. Boone J, Velazquez O, Cherry S. Small-animal X-ray dose from micro-CT. Mol Imaging. 2004;3(3):149. [PubMed: 15530250]

32. Miyahara N, Kokubo T, Hara Y, Yamada A, Koike T, Arai Y. Evaluation of X-ray doses and their corresponding biological effects on experimental animals in cone-beam micro-CT scans (R-mCT2). Radiol Phys Technol. 2016;9(1):60–68. [PubMed: 26441335]

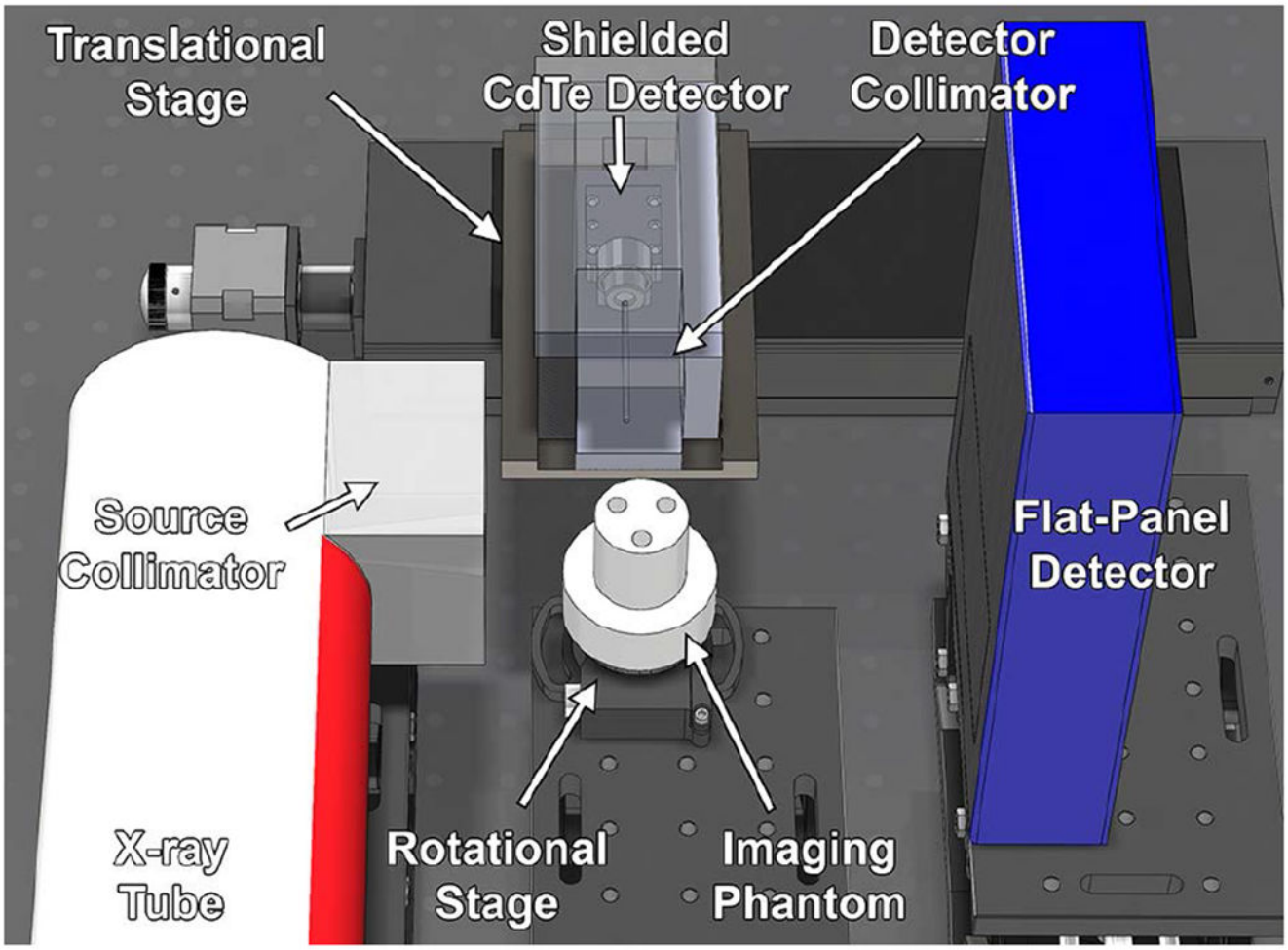

Figure 1.
Model of benchtop XFCT system showing major components (x-ray tube, source collimator, rotational stage, imaging phantom, shielded CdTe detector, detector collimator, translational stage, and flat-panel detector).

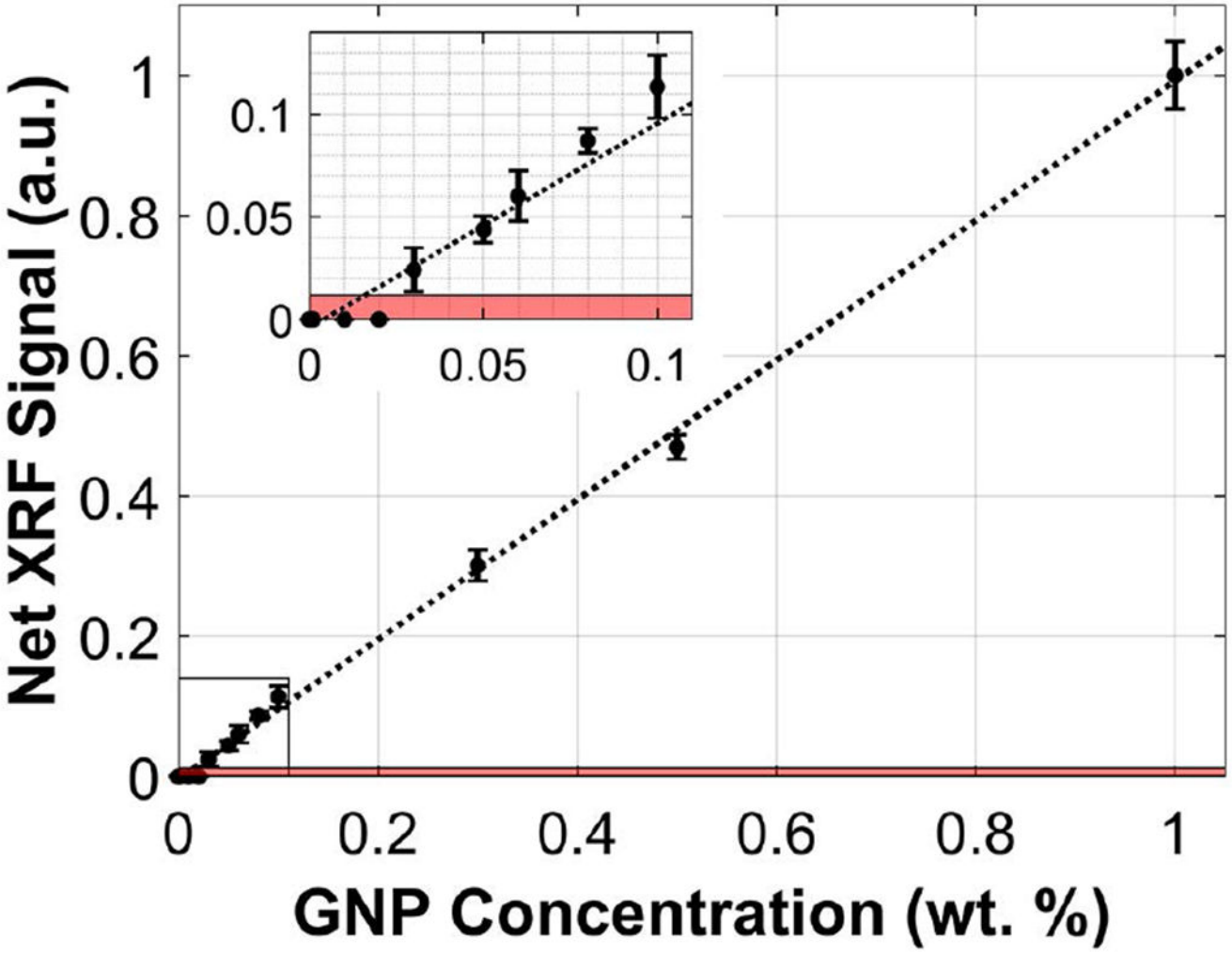

Figure 2.

Calibration curve depicting the net XRF signal (a.u., arbitrary units) as a function of GNP concentration at 0, 0.01, 0.02, 0.03, 0.05, 0.06, 0.08, 0.1, 0.3, 0.5, and 1.0 wt. %. The source was operated at 125 kVp, 24 mA with a 1.8-mm Sn filter. The XRF signal acquisition time was 10 s. The shaded area represents signal less than 1.96 times the standard deviation of the background (noise level). The lowest GNP concentration that was definitively detectable under these irradiation conditions was 0.03 wt. % or 0.3 mg/cm^3.

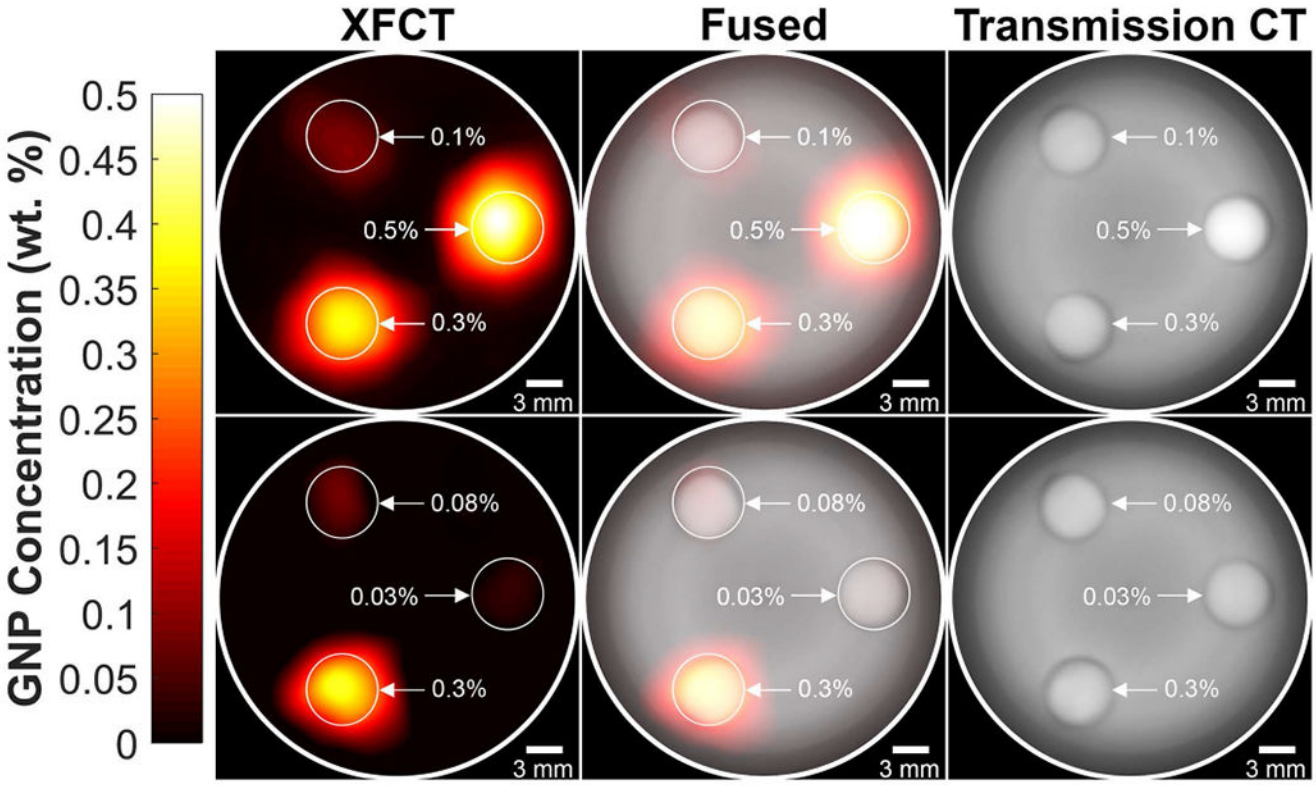

Figure 3.

Reconstructed and smoothed XFCT (left column), transmission CT (right column), and fused (middle column) images of 3-cm-diameter PMMA phantom under both the “high” (top row) and “low” (bottom row) configurations. The concentrations of the GNP/PBS inserts for the “high” configuration were 0.1, 0.3, and 0.5 wt. % and 0.03, 0.08, and 0.3 wt. % for the “low” configuration.

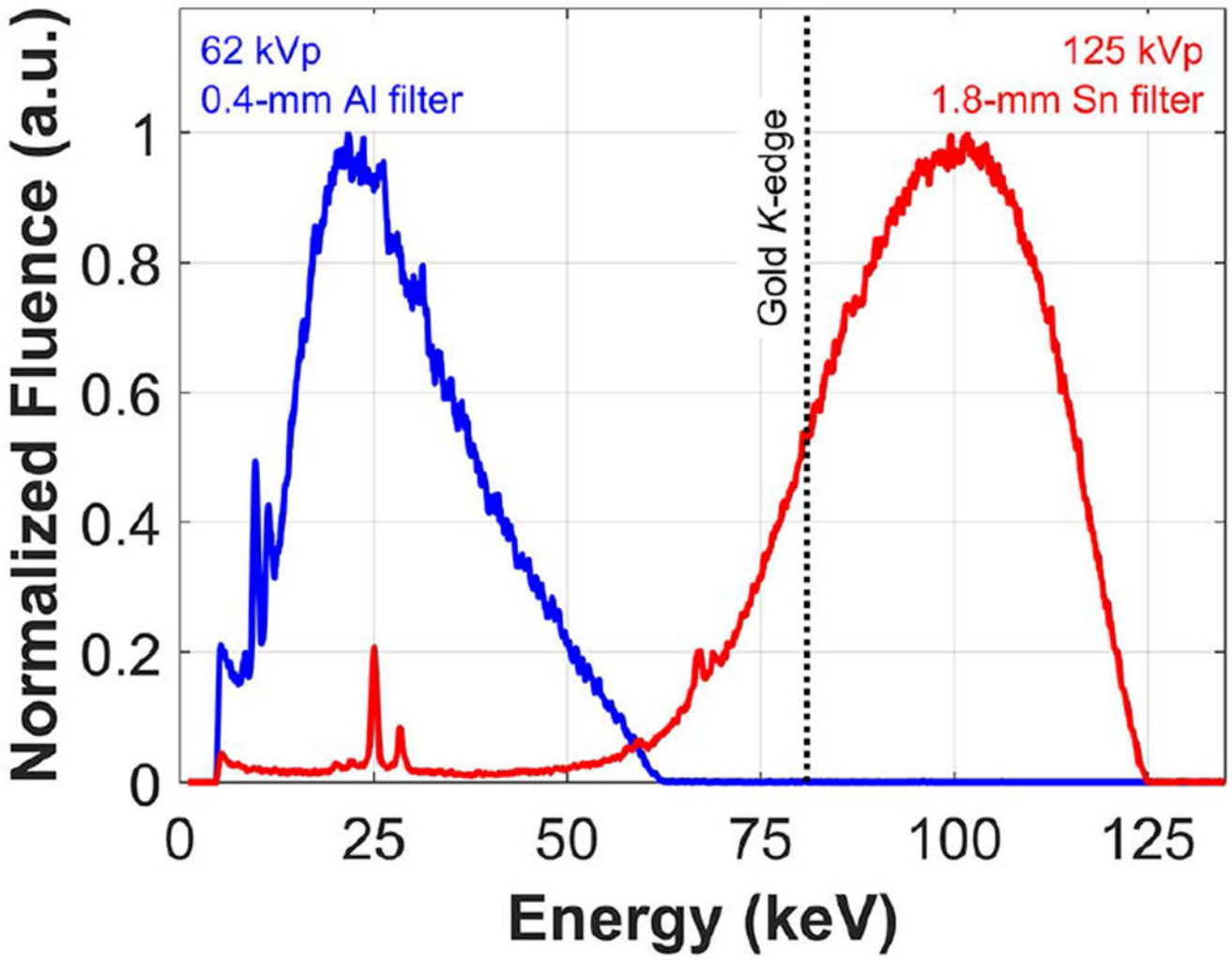

Figure 4.
Incident x-ray spectra used for XFCT (125 kVp, 1.8-mm Sn filter) and transmission CT (62 kVp, 0.4-mm Al filter) imaging. Fluence has been normalized to the maximum value for each spectrum to aid qualitative comparison.

Table 1.

Tabulated contrast-to-noise ratio (CNR) for various GNP concentrations based on XFCT and transmission CT images of the “high” and “low” phantom configurations.

GNP Concentration (wt. %)	Contrast-to-Noise Ratio (CNR)	
	XFCT	Transmission CT
	“High” Configuration[a]	
0.1	6.04	2.94
0.3	12.6	3.14
0.5	14.5	4.77
	“Low” Configuration[b]	
0.03	3.71	2.43
0.08	5.39	2.87
0.3	12.6	3.15

[a]Concentrations of GNP/PBS inserts for the “high” configuration were 0.1, 0.3, and 0.5 wt. %

[b]Concentrations of GNP/PBS inserts for the “low” configuration were 0.03, 0.08, and 0.3 wt. %

Table 2.

Dose rate and imaging dose metrics for XFCT and transmission CT configurations

	XFCT	Transmission CT
Incident X-ray Spectrum	125 kVp, 1.8-mm Sn	62 kVp, 0.4-mm Al
Dose Rate at Isocenter (cGy/min)	24.9 @ 24 mA	40.2 @ 1.0 mA
Acquisition Time per Projection (s)	10	0.05
Dose per Projection (cGy)	1.87 (effective)	0.0335
Total Number of Projections	330	360
Total Imaging Dose (cGy)	617 (effective)	12.1